Magnetic Signature in Graphene Using Adsorbed Metal–Organic Networks

Alain Rochefort, Khalid N Anindya, Xavier Bouju, Adam H Denawi

Magnetic Signature in Graphene Using Adsorbed Metal–Organic Networks

Alain Rochefort,[1]* Khalid N. Anindya,[1] Xavier Bouju,[2] and Adam H. Denawi[2,3]

1 - Département de génie physique, Polytechnique Montréal, H3C 3A7 Québec, Canada

2 - Centre d'élaboration de matériaux et d'études structurales, CEMES-CNRS, UPR 8011, Université de Toulouse 3Paul Sabatier, F-31055 Toulouse, France

3 - LPICM, CNRS, Ecole Polytechnique, IP Paris, 91128 Palaiseau, France

* Email: alain.rochefort@polymtl.ca

J. Phys. Chem. C 2024, 128, 919–926 — https://doi.org/10.1021/acs.jpcc.3c06657

ABSTRACT: The interaction of a 2D metal–organic network (MON) stacked on graphene has been studied with the help of first-principles density functional theory (DFT) and DFT+*U* calculations. By varying the length of a polyphenyl-dicarbonitrile linker, we have evaluated the influence of the metal–metal distance on the electronic and magnetic properties of the MON complexes. Although MON composed of small molecules shows a moderately stable ferromagnetic phase, this magnetic order drops with the size of the complex. After the adsorption of MON on graphene, this last becomes n-doped due to an important charge transfer that improves with the molecular unit size. The MON–graphene interaction contributes to drastically reduce the overall stability of any magnetic order, but the local charge transfer remains strongly spin-polarized-dependent. Hence, the adsorption of magnetic MON on graphene leads to the modification of the electronic and magnetic properties of graphene, mostly in a closed proximity region to the active metal atoms of the MON. Spin-polarized scanning tunneling microscopy simulations reveal a magnetic signature in graphene that originates from its interaction with the MONs and that could be experimentally observed.

INTRODUCTION

The creation of a highly ordered array of atom-based magnets remains a key element in the development of ultimate spintronics devices [1-3]. There are a few examples where a controlled deposition of magnetic atoms on a surface has been performed, but where the temperature has been shown to play a central role on the atomic arrangement stability and the lifetime of magnetic properties [4,5]. In contrast, on-surface synthesis (OSS) represents one of the most promising approaches to generate extended two-dimensional (2D) materials where the central coordination sites are metallic atoms [6-10]. By carefully designing the ligands, one can use OSS to synthesize a plethora of 2D arrays where metal atoms are organized into a specific shape with a well-defined distribution and physical properties [11,12]. Following such an approach, 2D metal–organic networks (MONs) have been prepared on various substrates such as transition metals (TMs), semi-conductors (SCs) including graphene, and insulator (IN) surfaces [13,14] as well as on stacked heterostructures (TM/TM, SC/TM, IN/TM, etc.) [15,16].

The electronic and magnetic properties of metal atoms in MONs strongly depend on the metal–ligands interactions within the complexes and are also significantly influenced by their subsequent interactions with the substrate [17]. For example, Cu can become magnetic when bonded to thiols [18] or adsorbed on graphene [19,20], while Ni can lose its magnetic character once it is adsorbed on graphene [19]. Hence, although the MON constitutes a very interesting alternative to control the distribution of metal atoms in space, we can hardly predict the electronic and magnetic properties of the metallic moieties without a careful analysis of the entire adsorbed

MON. Beyond the interest in the electronic and magnetic properties of the ordered metal arrays, the influence of the adsorbate on the properties of the substrate could also be of interest. For example, the adsorption of organic self-assembly or MON could be used to modify both the electronic and magnetic properties of graphene. On the other hand, magnetism can be induced into graphene alone by the presence of structural defects, deformation, and doping [21-23], but this weak effect can be efficiently screened by the presence of a metallic substrate or an increasing temperature [23]. Again, the adsorption of a MON on graphene appears quite appealing since it remains the less invasive way to modify the properties of graphene, while the MON–graphene interactions can be quite significant.

The aim of the present study is to determine the capability of MON-containing magnetic atoms (Co) to induce spin-polarized electronic states into graphene (G) in a non-invasive fashion and to evaluate the persistence of the magnetic characteristics of the MONs. Our computational approach considers the isolated species to describe the electronic and magnetic properties of individual MONs, first to estimate the influence of the Co–Co distance, second to describe their electronic properties, and third to evaluate the stability of different ordered magnetic phases. Then, for the MON/G complexes, we focus on the description of the interactions, the influence of graphene on the variation of magnetic properties including the exchange coupling between Co atoms, and the effect of MON adsorption on graphene properties.

COMPUTATIONAL METHODS

The DFT electronic structure calculations were performed using the Siesta [24] package (version 4.1.5). We used periodic boundary conditions with the well-known functional of Perdew–Burke–Ernzerhof (PBE) [25] in conjunction with van der Waals (vdW) corrections derived by Grimme [26], also known as the PBE+D2 approach. The computations were performed with norm-conserving Trouillier–Martins pseudo-potentials and double-ζ polarized atomic basis sets. The mesh cutoff used to form the real space grid in the DFT calculations was 500 Ry, and the structural relaxation and geometry optimization were carried out using the conjugate-gradient method until the forces and the variation of total energy were less than 0.01 eV/Å and 10^{-5} eV, respectively. We considered a vacuum region of 30 Å to minimize the interactions between periodic images in the direction normal to the slab. All optimizations were performed at Γ-point (*k*-point grid of 1×1×1), and all the properties were obtained with a 9×9×1 *k*-point grid. A Bader charge analysis was undertaken with the Bader code developed by the Henkelman group [27]. The simulations of STM images were carried out at the Tersoff–Hamann level of theory [28], and the topography images were obtained at constant height mode. In all spin-polarized STM images, the contrast corresponds to the variation of the spin density component normal to the MON+graphene surface.

The adsorption of the different MONs on graphene was modeled by considering three polyphenyl-based molecules linked to two cobalt (Co) atoms and where the Co atoms occupy on-top adsorption sites on the graphene substrate. It is noteworthy that the most stable position of a single Co atom on the graphene surface has been a source of debate over a long period of time [29-41]. It appears that the relaxation of graphene during adsorption may lead to different stable positions of Co on graphene: for the unrelaxed case, the most favorable adsorption site is the hollow site (the middle of a hexagon on graphene), whereas the on-top site (on top of a C atom) is privileged for a relaxed graphene sheet. This latter position is also found by considering a Hubbard correction, as one will see in the following. The different unit cells used for the calculations are reported in Figure 1, where C1, C2, and C3 have, respectively, one, two, and three phenyl rings within the *para*-polyphenyl-dicarbonitrile (NC–CX–CN) building block. The size of the graphene substrate unit cell was adapted to fit the size of the MONs that form a hexagonal arrangement with increasing pore size from C1 (2.27 nm) to C3 (3.98 nm), as shown for the C1 system in Figure 1. For the geometry optimization procedure, we first optimized the different free-standing graphene substrates containing 128 (C1), 242 (C2), and 392 (C3) carbon atoms. Since the geometry of graphene is quite robust and very weakly perturbed by the presence of an adsorbed MON phase, we then used those optimized graphene substrates on which the adsorbed MONs were fully optimized, while graphene was fixed. In all the optimization procedures, the

contribution from vdW interactions to the total energy was considered by using the D2 approach [26].

In order to evaluate the magnetic coupling between Co atoms within a single MON, in other words, to evaluate the exchange coupling constant ($J \approx E_{AFM} - E_{FM}$) by comparing the total energy of antiferromagnetic (AFM) and ferromagnetic (FM) phases, we have adopted a similar procedure to Pétuya and Arnau [42] that consists in using the optimized non-spin-polarized structure for calculating the spin-polarized total energy of AFM and FM phases. To validate this approximation, we performed closed-shell and open-shell DFT calculations on the C1/G system to compare the geometry of the optimized structures. The most noticeable change observed in the optimized geometry from the closed-shell to the FM states is a small out-of-plane displacement of the nitrogen atoms by 0.18 Å, which represents a 6% variation with respect to the original closed-shell value. Moreover, such a change implies an elongation of the Co–N bond distance of 0.07 Å, corresponding to a variation of 4%. All the remaining C1 backbones, including Co atoms, do not show any significant differences from the closed-shell to the open-shell (FM) structures. Although such small deformations would not have a significant impact on the electronic structure properties of a given magnetic phase, this small geometry variation could contribute to the total energy of the systems by a significant amount with respect to the exchange coupling energy. Then, in order to minimize this contribution from relaxation energy in the estimation of exchange energy, it appears quite realistic to fix the geometry to compare the total energy of AFM and FM for evaluating exchange energy. Following this strategy [42], the difference in total energy between AFM and FM phases can be more directly attributed to a change in their spin density distributions rather than to the influence of structural relaxation on the stability of the magnetic phases. Hence, all of the spin-polarized calculations were performed on fixed geometries after a full relaxation of the closed-shell systems.

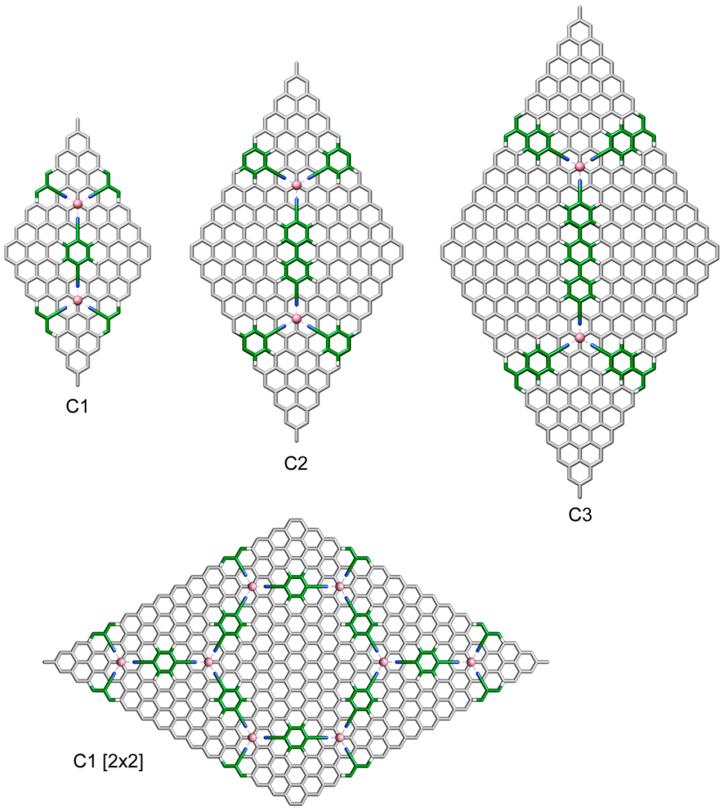

Figure 1*. Unit cells that model the adsorption of MONs made of para-polyphenyldicarbonitrile molecules and cobalt atoms on a graphene (G) substrate. The top images give the structure of MON units containing one to three phenyl rings (C1 to C3) and the bottom image shows a (2×2) array of the C1/G unit cell. Green and gray color atoms are C, blue are N, pink are Co, and white are H atoms.*

To better describe the relative stability of FM and AFM phases of the MONs, we performed additional spin-polarized calculations beyond the generalized-gradient functional (GGA) limits using Siesta [24] and Quantum ESPRESSO (QE) [43-44] packages with the DFT+*U* method. The Siesta package allows investigating larger systems than QE but is often considered to be less accurate due to the use of a localized atomic orbital basis rather than plane waves as in QE. With QE, we applied DFT+*U* corrections from the more recent formulation of Himmetoglu et al. [45] for cobalt (Co), with $U = 5$ eV. Such a *U* value with metal–organic compounds containing TM ions was successfully used for many compounds such as TM–(Fe-tetracyanobenzene) [46], TM–(7,7,8,8-tetracyanoquinodimethane) [47], and TM–(zwitterionic quinone) [48,49]. The interaction between the valence electrons and ionic cores was described within the framework of the projector-augmented wave (PAW) method. The electronic wave functions were expanded in plane waves with a kinetic energy cutoff of 500 eV and a grid of (2×2×1) points. We validated our DFT+*U* approach by using different approaches on a small C1/G system to reproduce the *J* value obtained from the PBE0 hybrid-functional. Although PBE0 is considered the most accurate approach to determine the magnetic ground state of a system, its use for large systems is much less computationally practical within a reasonable timeframe. More details on this DFT+*U* validation procedure are reported in the Supporting Information and Table S1.

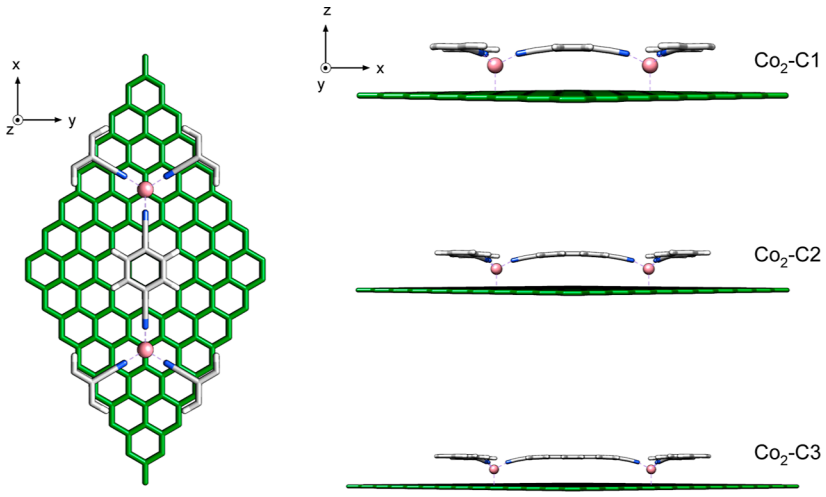

***Figure 2**. Optimized structures of the C1 to C3 complexes on graphene show a strong interaction of the Co atoms with the substrate.*

RESULTS AND DISCUSSION

Spin-Density Distribution in MON/G Complexes. The geometry of the graphene substrate is not significantly altered by the adsorption of MONs, but the electronic structure of this last is quite perturbed, especially in the vicinity of the Co moieties. Figure 2 shows side views of the optimized complexes where the Co atoms have significantly plunged toward the graphene surface, while the bonded polyphenyl groups have become highly bent. In such configuration, the short Co–graphene distance (d_{Co-G}) slightly decreases from 2.12 to 2.03 Å from C1 to C3 complexes, while the polyphenyl fragments are repelled up to ~3.25 Å above the graphene surface, i.e., in the same range as for vdW distances observed for aromatic molecules adsorbed on graphene [50,51]. In addition, due to the strong interactions between Co atoms and the terminal CN groups, the polyphenyl fragments near Co atoms are more strongly deformed.

Table 1 summarizes the electronic and magnetic properties of the different complexes considered. In order to estimate the influence of graphene on the MON properties, we will first discuss the properties calculated for isolated MONs with similar geometry to the adsorbed cases. Those calculated values are reported in parentheses in Table 1. The total magnetization (*S*)

calculated for freestanding C1 to C3 complexes clearly indicates a magnetic character, and the exchange coupling energy (J), simply expressed here as the energy difference between AFM and FM phases, shows that the ground states are slightly FM. Nevertheless, the low magnitude of J (close to thermal energy, $k_B T$) and its decreasing nature from C1 to C3 suggest a weaker magnetic order with a complex size. While most of the charge transfer occurs from the Co atoms to the CN moieties, there is also a significant amount of charge that is transferred from the polyphenyl fragments to the CN groups. Since the MONs are slightly bent along the z-direction, this charge transfer leads to the appearance of an out-of-plane dipole moment.

If we now turn to the MON/G complexes, the total energies for the ground states also indicate magnetic behavior. The calculated exchange-coupling parameter J generally remains quite small at both DFT and DFT+U levels. The determination of ground states for such weakly spin-ordered systems is quite delicate and remains highly challenging. In fact, we have explored several approaches to determine the value of J for the C1/G complex, which leads to a multitude of ground states with relatively small absolute energy differences (see Table S1). Moreover, we observed that the DFT+U+J approach that was successfully used for complexes with significant exchange coupling is much less reliable for describing MON/G systems in which the exchange coupling is much smaller (see Figure S1 in Supporting Information). All calculated absolute values of J for the MON/G complexes are lower than 7 meV; we can then safely attribute a paramagnetic behavior to those complexes in practical conditions. From a magnetic perspective, we observe that the presence of graphene reduces the total magnetization of MONs by 30– 50%, but it also contributes to a significant decrease in the exchange coupling energy.

In contrast, the variation of electronic properties related to charge density is quite remarkable. For example, the Bader analysis indicates a significant fluctuation of charges within the MONs but, more importantly, between the MONs and graphene. Graphene becomes negatively charged or, in other words, n-doped, and the amount of charge accumulation on graphene increases with the MON size. Given the proximity of Co atoms to graphene, we may anticipate that most of the substrate n-doping originates from the Co-to-graphene charge transfer. Table 1 indicates a similar charge accumulation on graphene for both the AFM and FM phases, suggesting that the magnitude of the charge transfer is not directly related to the magnetic character of the complexes. The net positive charges on Co atoms remain nearly constant among the different complexes; however, we observe an increasing amount of negative charges on graphene, while the net electron charges on the carbonitrile moieties decrease with the size of the MON. Upon MON adsorption onto graphene, the fluctuation of charges on Co atoms and CN groups from the isolated complexes does not clearly depend on the building block length; Co atoms provide an additional $\sim$0.25 e, while CN groups give around $\sim$0.40 e in all complexes. Beyond this $\sim$0.65 e charge transfer from the "Co_2–$(CN)_6$" moiety to graphene, an additional charge transfer from the polyphenyl backbone is required to explain the increasing amount of negative charge on graphene with the size of the MONs. In fact, although the net negative charge increases on graphene from C1 to C3 complexes, we observe that its relative doping level decreases from 0.007 e/C atom to 0.004 e/C atom from C1 to C3. This last result indicates that doping is limited to the region in the closed vicinity with the molecular backbone of the MONs. Finally, the large dipole moment (μ_D) calculated for the MON/G complexes agrees very well with the increasing amount of negative charge transferred to graphene with the MON size.

Table 1. Spin-Density Properties of MONs Adsorbed on Graphene[a]

system	J (meV)		ΔE (eV)	Bader charge |e|						S (FM)	μ_D (Debye) (FM)
	DFT	DFT + U		Co-1 + Co-2		graphene		$(-CN)_6$			
				AFM	FM	AFM	FM	AFM	FM		
Co_2–C1	−1.0 (33)	5.0 (27)	2.09	2.10 (1.88)	2.06 (1.92)	−0.89	−0.89	−2.62 (−2.98)	−2.55 (−2.98)	3.00 (5.98)	4.33 (2.01)
Co_2–C2	−6.6 (47)	2.3 (19)	2.32	2.09 (1.85)	2.09 (1.87)	−1.18	−1.17	−2.28 (−2.64)	−2.28 (−2.63)	4.18 (5.98)	7.37 (2.45)
Co_2–C3	0.2 (30)	1.4 (9)	2.47	2.20 (1.96)	2.20 (1.98)	−1.47	−1.47	−1.70 (−2.10)	−1.70 (−2.09)	3.97 (5.96)	10.05 (2.58)

[a]*The exchange coupling energy, $J \approx E_{AFM} - E_{FM}$ (in meV), was calculated at the PBE+D2 (DFT) level with Siesta and at the DFT + U level with QE. ΔE is the energy (in eV) of the non-polarized state with respect to the ground state. The Bader charges, the total magnetization (S), and the net dipole moment (μ_D) were evaluated at the PBE+D2 level. All values in parentheses are for the isolated MON. All calculations include a D2 correction for vdW interactions.*

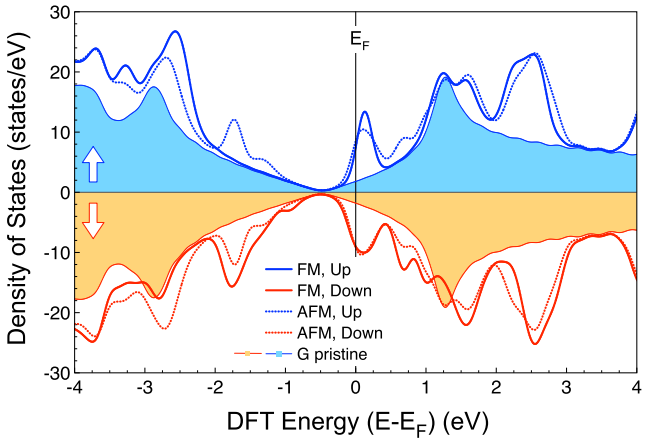

Figure 3. *DOS of different magnetic phases of the C1/G complex. The DOS of pristine graphene (dotted lines) is shown for reference.*

Electronic Structure Properties of MON/G Complexes. The comparison of density of states (DOS) between AFM (dashed lines with filled area) and FM (solid curves) phases for the C1/G complex is shown in Figure 3 for both up (blue curves) and down (red curves) spins with respect to pristine graphene (dotted lines). Although the DOS of both phases indicates that graphene clearly becomes n-doped upon the adsorption of C1, we observe major electronic structure differences near the Fermi level. First, the Fermi level is pinned well above the neutrality point of graphene (around −0.5 eV from E_F[G]). Second, there is a significant amount of mixing of states below and above the neutrality point of graphene and, more importantly, at the Fermi level. With respect to pristine graphene, the AFM state (filled curves) shows additional states between −2 and −0.5 and +1.0 and −0.5 eV, in the valence and the conduction band, respectively. Here, to mention, the AFM state exhibits degenerate eigenstates for both spins. As for the FM phase, we also observe an important mixing of states in these energy regions, but mostly for down spin density, for which the DOS at the Fermi level is even higher than that for up spin density.

A more detailed description of states mixing near the Fermi level is reported in Figure 4 for the AFM phase. Since the distribution of states is symmetric for up and down spins in the AFM phase, we show only the projected DOS (PDOS) for the up spin for clarity. It is interesting to note that states at the Fermi level mostly originate from the mixing of graphene and polyphenyl backbone states including Co–$(CN)_3$ fragments, while the larger contribution from Co atoms near E_F is located in the valence band between −2 and −1 eV. Co atoms also moderately mix with

graphene at E_F, and the magnitude of variations observed from pristine graphene to graphene in C1/ G between 0 and +1 eV is about the same as the contribution from Co atoms (between −2 and −1 eV). The mixing of states between graphene and MONs at the Fermi level and between 0 and −1 eV demonstrates that the electronic structure of the graphene substrate is significantly modified by the presence of the adsorbed MON.

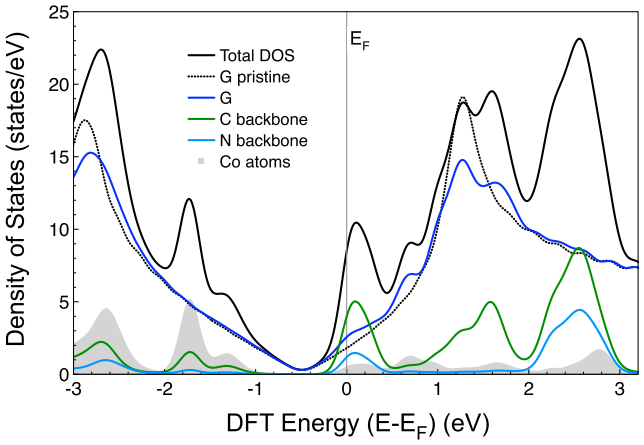

***Figure 4**. PDOS for the different atomic species in the C1/G complex.*

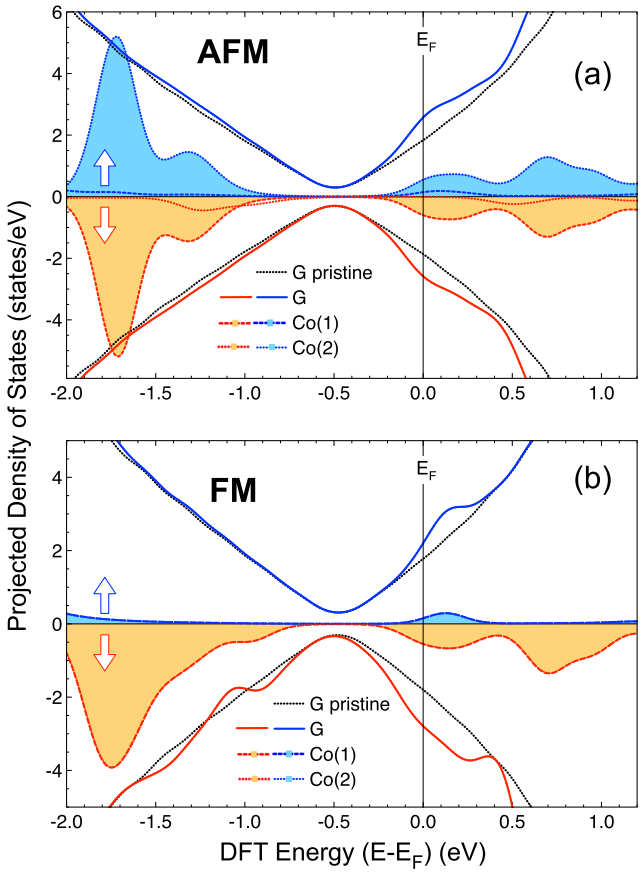

***Figure 5**. Comparison of the spin-polarized PDOS of graphene and Co atoms in the C1/G complex. The DOS of pristine graphene is reported for both (a) AFM and (b) FM phases for reference.*

In order to describe the relationship between Co atoms and graphene in their states-mixing region near E_F, Figure 5 compares the PDOS of graphene and Co atoms for the AFM and FM phases of the C1/G complex. To emphasize the role of individual Co atoms in the spin density of the complexes, we have considered the projection of each Co atom and have included the DOS of pristine graphene for comparison. In fact, although the contribution from Co atoms is lower at E_F than between −2 and −1 eV, we can clearly observe a larger perturbation of the electronic structure of graphene at E_F for both AFM and FM phases. Beyond a small spin contamination [52], we can clearly differentiate the spin density on each Co atom in the AFM phase (spin down = Co-1 and spin up = Co-2). Most of the electronic structure perturbation in graphene is observed at E_F for up and down spins — symmetrically for AFM and more significantly for down spin states in the FM phase. This result indicates a specific interaction of magnetic Co atoms with the graphene substrate, but that could not give a well-ordered magnetic phase at room-temperature conditions. A similar behavior is observed for larger MONs; Figure 6 shows the projection of Co atoms and graphene from the different complexes according to the AFM and FM phases.

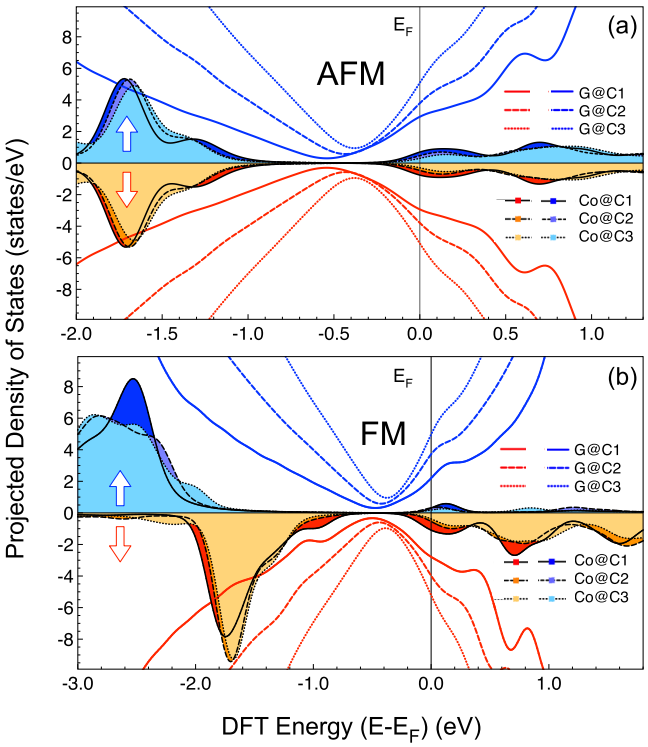

***Figure 6**. Comparison of the spin-polarized PDOS of graphene and Co atoms from C1/G to C3/G complexes for both (a) AFM and (b) FM phases.*

The trends observed for graphene and Co atoms are very similar in both the AFM and FM phases. From C1 to C3, the neutrality point of graphene is shifted toward the Fermi level, supporting a decreasing n-doping (per C atom) with a larger MON size, as discussed above. A decreasing contribution of Co atoms at the Fermi level is observed from C1 to C3 complexes as well as less apparent perturbations of graphene electronic structure with the MON size. The increasing PDOS splitting of the neutrality point for up and down spins just below E_F from C1 to C3 complexes is related to the increasing size of the graphene substrate. In fact, larger models produce larger amounts of states around E_F, and those become increasingly convoluted as the substrate size increases due to the broadening factor used to generate the DOS profiles. Figure S2 (see Supporting Information) clearly demonstrates that this neutrality point splitting is related to the substrate size and not to a bandgap opening induced by the MON; the freestanding (G[Cx]) and stacked graphene (G−Cx) models give rise to exactly the same amount of DOS at the neutrality point, which increases with graphene size.

In order to investigate the local electronic and magnetic properties of graphene within the stacked heterostructure, we performed spin-polarized STM simulations on the backplane of the complexes, just underneath the graphene plane, to emphasize the direct influence of the MONs on graphene. Figure 7 compares the STM images of the AFM and FM phases of the C1/G complex, the calculated image for a single cell, and an arrangement of (3×3) cells to emphasize the electronic and magnetic patterns induced in graphene.

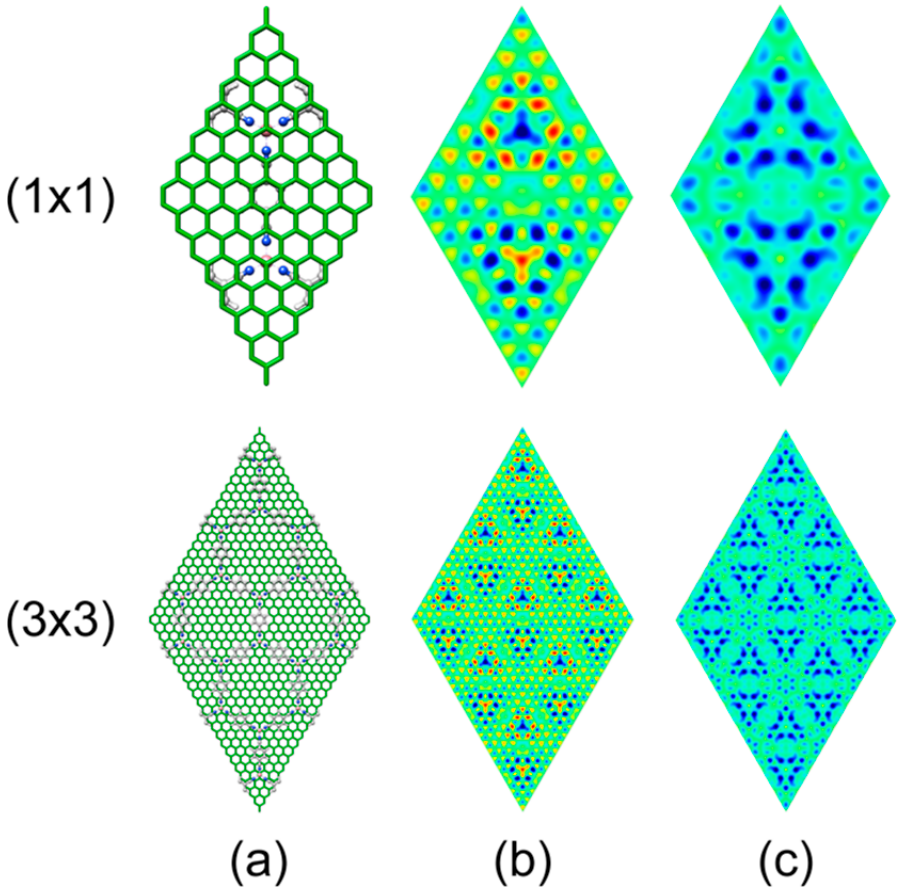

***Figure 7**. Spin-polarized simulations of STM images for (a) single (1×1) and multiple (3×3) unit cells of the C1/G complex for (b) AFM and (c) FM phases. The out-of-plane component of the spin density was used to generate the STM image underneath graphene in the C1/G complex. V = −0.2 V, scale: -1×10^{-5} (blue) to $+1 \times 10^{-5}$ (red).*

The scanning tunneling microscopy (STM) images of the AFM phase clearly show a spin-density localization on carbon atoms near Co atoms from the MON, specifically on atoms not only directly bonded to Co but also the next C atoms. Beyond this small zone, we observe a fluctuation of the spin density from a C atom to the next one, which gradually decreases in magnitude as the distance from the Co atoms increases. Surprisingly, the highest spin-density magnitude appears on C atoms with opposite spin to the spin-density induced directly from Co atoms. This phenomenon is clearly visible for the FM phase where down spin density dominates over the entire domain. As observed in Figure 5, down spin density is strongly dominant at low voltages below the Fermi level. Larger-scale STM images allow us to observe that Co atoms induce different spin-density patterns in graphene, which are partially overlapping through spin-dependent evanescent-induced states (see also Figures S3 and S4, Supporting Information). Our DFT calculations revealed that the adsorption of MONs led to a lower exchange coupling J value to a point where no magnetic coupling is expected. Nevertheless, STM images clearly indicate an influence of the magnetic Co atoms on both the electronic and magnetic properties of graphene. Then, the interactions of Co atoms within the MON generate n-doping of graphene, and this doping is spin-polarized (see

Figure S5). To summarize the interaction of magnetic MONs with graphene, Figure 8 shows the influence of the spin-polarized charge transfer on the variation of the net electric (μ_D) and magnetic (μ_B) dipole moments considering the AFM coupling between the MON and graphene. The charge transfer from Co atoms to graphene invariably induces an increasing dipole moment for both the AFM and FM phases. In contrast, due to an AFM coupling of Co atoms to graphene, the spin-polarized charge transfer contributes to decrease the magnetic moment of the FM phases (red arrows) but has no influence on the magnetic moment of the AFM phase (green arrows).

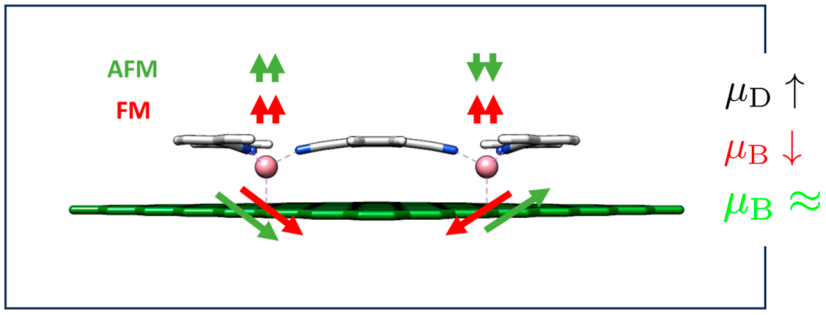

***Figure 8**. Influence of the charge transfer on the electronic and magnetic properties of MON/G complexes.*

CONCLUSIONS

In this work, we have shown that the adsorption of magnetic MONs on graphene induces magnetic and electronic perturbation of the substrate. First, graphene becomes n- doped due to a significant charge transfer from the MON moiety, where a significant mixing of states between the metal atoms from the MON and carbon atoms of graphene is observed. Second, graphene contributes to partially screen the magnetic behavior of the adsorbed MON through an AFM coupling. Beyond decreasing the magnetic moment of the systems, this coupling creates a clear spin-density polarization in graphene. Although the magnetic order in all MON/G complexes remains relatively weak, spin-polarized STM simulations clearly demonstrated a magnetic signature in the electronic structure of graphene. The AFM coupling between Co atoms in MONs decreases from C1 to C3 as the separation between Co atoms in the networks becomes nearly negligible once the MONs are adsorbed on graphene. This work opens the route to the creation of magnetic and electronic patterns in graphene and other 2D materials.

Supporting Information

Determination of the ground state for C1/G systems using different DFT+*U* approaches, PDOS near the Fermi level of graphene in the absence and in the presence of the adsorbed MON, calculated spin-polarized STM images of the C1/G complex at different heights among the stacks for the AFM phase, calculated spin-polarized STM images of the C1/G complex at different heights among the stacks for the FM phase, and height profile across a single unit cell of the C1/G system for the FM and AFM phases.

ACKNOWLEDGMENTS

A.R. and K.N.A. acknowledge the financial support from the Natural Sciences and Engineering Research Council of Canada (NSERC) through the Discovery grant program, and K.N.A. is grateful to FRQNT for providing a scholarship through the PBEEE program. A.H.D. and X.B. mention that this study has been (partially) supported through the EUR grant NanoX no. ANR-17-EURE-0009 in the framework of the “Programme des Investissements d’Avenir”. We thank the Digital Research Alliance of Canada (the Alliance) and Calcul Québec for providing computational resources and support. This work was granted access to the HPC resources of the CALMIP supercomputing center under the allocation 2021-P0832.

REFERENCES

(1) Bennewitz, R.; Crain, J. N.; Kirakosian, A.; Lin, J.-L.; McChesney, J. L.; Petrovykh, D. Y.; Himpsel, F. J. Atomic scale memory at a silicon surface. *Nanotechnology* **2002**, *13*, 499–502.

(2) Bogani, L.; Wernsdorfer, W. Molecular spintronics using single-molecule magnets. *Nat. Mater.* **2008**, *7*, 179–186.

(3) Thorarinsdottir, A. E.; Harris, T. D. Metal–Organic Framework Magnets. *Chem. Rev.* **2020**, *120*, 8716–8789.

(4) Loth, S.; Baumann, S.; Lutz, C. P.; Eigler, D. M.; Heinrich, A. J. Bistability in Atomic-Scale Antiferromagnets. *Science* **2012**, *335*, 196–199.

(5) Baltic, R.; Pivetta, M.; Donati, F.; Wäckerlin, C.; Singha, A.; Dreiser, J.; Rusponi, S.; Brune, H. Superlattice of Single Atom Magnets on Graphene. *Nano Lett.* **2016**, *16*, 7610–7615.

(6) Barth, J. V.; Costantini, G.; Kern, K. Engineering atomic and molecular nanostructures at surfaces. *Nature* **2005**, *437*, 671–679.

(7) Lin, N.; Barth, J. V. Surface-Confined Supramolecular Coordination Chemistry. *Top. Curr. Chem.* **2009**, *287*, 1–44.

(8) Dong, L.; Gao, Z.; Lin, N. Self-assembly of metal–organic coordination structures on surfaces. *Prog. Surf. Sci.* **2016**, *91*, 101– 135.

(9) Bouju, X.; Mattioli, C.; Franc, G.; Pujol, A.; Gourdon, A. Bicomponent Supramolecular Architectures at the Vacuum–Solid Interface. *Chem. Rev.* **2017**, *117*, 1407–1444.

(10) Clair, S.; de Oteyza, D. G. Controlling a Chemical Coupling Reaction on a Surface: Tools and Strategies for On-Surface Synthesis. *Chem. Rev.* **2019**, *119*, 4717–4776.

(11) Chakraborty, G.; Park, I.-H.; Medishetty, R.; Vittal, J. J. Two- Dimensional Metal-Organic Framework Materials: Synthesis, Struc- tures, Properties and Applications. *Chem. Rev.* **2021**, *121*, 3751–3891.

(12) Yan, X.; Su, X.; Chen, J.; Jin, C.; Chen, L. Two-Dimensional Metal-Organic Frameworks Towards Spintronics. *Angew. Chem., Int. Ed.* **2023**, *62*, No. e202305408.

(13) Schlickum, U.; Decker, R.; Klappenberger, F.; Zoppellaro, G.; Klyatskaya, S.; Ruben, M.; Silanes, I.; Arnau, A.; Kern, K.; Brune, H.; et al. Metal-Organic Honeycomb Nanomeshes with Tunable Cavity Size. *Nano Lett.* **2007**, *7*, 3813–3817.

(14) Zhang, L. Z.; Wang, Z. F.; Huang, B.; Cui, B.; Wang, Z.; Du, S. X.; Gao, H.-J.; Liu, F. Intrinsic Two-Dimensional Organic Topological Insulators in Metal–Dicyanoanthracene Lattices. *Nano Lett.* **2016**, *16*, 2072–2075.

(15) Kumar, A.; Banerjee, K.; Foster, A. S.; Liljeroth, P. Two- Dimensional Band Structure in Honeycomb Metal–Organic Frameworks. *Nano Lett.* **2018**, *18*, 5596–5602.

(16) Li, J.; Solianyk, L.; Schmidt, N.; Baker, B.; Gottardi, S.; Moreno Lopez, J. C.; Enache, M.; Monjas, L.; van der Vlag, R.; Havenith, R. W. A.; et al. Low-Dimensional Metal−Organic Coordination Structures on Graphene. *J. Phys. Chem. C* **2019**, *123*, 12730−12735.

(17) Field, B.; Schiffrin, A.; Medhekar, N. V. Correlation-induced magnetism in substrate-supported 2D metal-organic frameworks. *npj Comput. Mater.* **2022**, *8*, 227.

(18) Garitaonandia, J. S.; Insausti, M.; Goikolea, E.; Suzuki, M.; Cashion, J. D.; Kawamura, N.; Ohsawa, H.; Gil De Muro, I.; Suzuki, K.; Plazaola, F.; et al. Chemically Induced Permanent Magnetism in Au, Ag, and Cu Nanoparticles: Localization of the Magnetism by Element Selective Techniques. *Nano Lett.* **2008**, *8*, 661−667.

(19) Cao, C.; Wu, M.; Jiang, J.; Cheng, H.-P. Transition metal adatom and dimer adsorbed on graphene: Induced magnetization and electronic structures. *Phys. Rev. B: Condens. Matter Mater. Phys.* **2010**, *81*, 205424.

(20) Manadé, M.; Viñes, F.; Illas, F. Transition metal adatoms on graphene: A systematic density functional study. *Carbon* **2015**, *95*, 525−534.

(21) Yazyev, O. V. Emergence of magnetism in graphene materials and nanostructures. *Rep. Prog. Phys.* **2010**, *73*, 056501.

(22) Tucěk,J.; Holá,K.; Bourlinos,A.B.; Błoński,P.; Bakandritsos, A.; Ugolotti, J.; Dubecký M.; Karlický F.; Ranc, V.; Čépe, K.; et al. Room temperature organic magnets derived from sp3 functionalized graphene. *Nat. Commun.* **2017**, *8*, 14525.

(23) Alimohammadian, M.; Sohrabi, B. Observation of magnetic domains in graphene magnetized by controlling temperature, strain and magnetic field. *Sci. Rep.* **2020**, *10*, 21325.

(24) Soler, J. M.; Artacho, E.; Gale, J. D.; García, A.; Junquera, J.; Ordejón, P.; Sánchez-Portal, D. The SIESTA method for ab initio order-*N* materials simulation. *J. Phys.: Condens. Matter* **2002**, *14*, 2745−2779.

(25) Perdew, J. P.; Burke, K.; Ernzerhof, M. Generalized Gradient Approximation Made Simple. *Phys. Rev. Lett.* **1996**, *77*, 3865−3868.

(26) Grimme, S. Semiempirical GGA-type density functional constructed with a long-range dispersion correction. *J. Comput. Chem.* **2006**, *27*, 1787−1799.

(27) Sanville, E.; Kenny, S. D.; Smith, R.; Henkelman, G. Improved grid-based algorithm for Bader charge allocation. *J. Comput. Chem.* **2007**, *28*, 899−908.

(28) Tersoff, J.; Hamann, D. R. Theory of the scanning tunneling microscope. *Phys. Rev. B: Condens. Matter Mater. Phys.* **1985**, *31*, 805−813.

(29) Chan, K. T.; Neaton, J. B.; Cohen, M. L. First-principles study of metal adatom adsorption on graphene. *Phys. Rev. B: Condens. Matter Mater. Phys.* **2008**, *77*, 235430.

(30) Mao, Y.; Yuan, J.; Zhong, J. Density functional calculation of transition metal adatom adsorption on graphene. *J. Phys.: Condens. Matter* **2008**, *20*, 115209.

(31) Sevinçli, H.; Topsakal, M.; Durgun, E.; Ciraci, S. Electronic and magnetic properties of 3d transition-metal atom adsorbed graphene and graphene nanoribbons. *Phys. Rev. B: Condens. Matter Mater. Phys.* **2008**, *77*, 195434.

(32) Krasheninnikov, A. V.; Lehtinen, P. O.; Foster, A. S.; Pyykkö, P.; Nieminen, R. M. Embedding Transition-Metal Atoms in Graphene: Structure, Bonding, and Magnetism. *Phys. Rev. Lett.* **2009**, *102*, 126807.

(33) Johll, H.; Kang, H. C.; Tok, E. S. Density functional theory study of Fe, Co, and Ni adatoms and dimers adsorbed on graphene. *Phys. Rev. B: Condens. Matter Mater. Phys.* **2009**, *79*, 245416.

(34) Wehling, T. O.; Balatsky, A. V.; Katsnelson, M. I.; Lichtenstein, A. I.; Rosch, A. Orbitally controlled Kondo effect of Co adatoms on graphene. *Phys. Rev. B: Condens. Matter Mater. Phys.* **2010**, *81*, 115427.

(35) Jacob, D.; Kotliar, G. Orbital selective and tunable Kondo effect of magnetic adatoms on graphene: Correlated electronic structure calculations. *Phys. Rev. B: Condens. Matter Mater. Phys.* **2010**, *82*, 085423.

(36) Chan, K. T.; Lee, H.; Cohen, M. L. Gated adatoms on graphene studied with first-principles calculations. *Phys. Rev. B: Condens. Matter Mater. Phys.* **2011**, *83*, 035405.

(37) Wehling, T. O.; Lichtenstein, A. I.; Katsnelson, M. I. Transition-metal adatoms on graphene: Influence of local Coulomb interactions on chemical bonding and magnetic moments. *Phys. Rev. B: Condens. Matter Mater. Phys.* **2011**, *84*, 235110.

(38) Liu, X.; Wang, C. Z.; Yao, Y. X.; Lu, W. C.; Hupalo, M.; Tringides, M. C.; Ho, K. M. Bonding and charge transfer by metal adatom adsorption on graphene. *Phys. Rev. B: Condens. Matter Mater. Phys.* **2011**, *83*, 235411.

(39) Rudenko, A. N.; Keil, F. J.; Katsnelson, M. I.; Lichtenstein, A. I. Adsorption of cobalt on graphene: Electron correlation effects from a quantum chemical perspective. *Phys. Rev. B: Condens. Matter Mater. Phys.* **2012**, *86*, 075422.

(40) Krychowski, D.; Kaczkowski, J.; Lipinski, S. Kondo effect of a cobalt adatom on a zigzag graphene nanoribbon. *Phys. Rev. B: Condens. Matter Mater. Phys.* **2014**, *89*, 035424.

(41) Wang, W.; Li, C.; Cao, J.; Fang, C. Adsorption Behaviors of Cobalt on the Graphite and SiC Surface: A First-Principles Study. *Sci. Technol. Nucl. Install.* **2017**, *2017*, 8296387.

(42) Pétuya, R.; Arnau, A. Magnetic coupling between 3d transition metal adatoms on graphene supported by metallic substrates. *Carbon* **2017**, *116*, 599–605.

(43) Giannozzi, P.; Baroni, S.; Bonini, N.; Calandra, M.; Car, R.; Cavazzoni, C.; Ceresoli, D.; Chiarotti, G. L.; Cococcioni, M.; Dabo, I.; et al. QUANTUM ESPRESSO: a modular and

open-source software project for quantum simulations of materials. *J. Phys.: Condens. Matter* **2009**, *21*, 395502.

(44) Giannozzi, P.; Andreussi, O.; Brumme, T.; Bunau, O.; Buongiorno Nardelli, M.; Calandra, M.; Car, R.; Cavazzoni, C.; Ceresoli, D.; Cococcioni, M.; et al. Advanced capabilities for materials modelling with Quantum ESPRESSO. *J. Phys.: Condens. Matter* **2017**, *29*, 465901.

(45) Himmetoglu, B.; Wentzcovitch, R. M.; Cococcioni, M. First- principles study of electronic and structural properties of CuO. *Phys. Rev. B: Condens. Matter Mater. Phys*. **2011**, *84*, 115108.

(46) Mabrouk, M.; Savoyant, A.; Giovanelli, L.; Clair, S.; Hayn, R.; Ben Chaabane, R. Ligand Influence on Local Magnetic Moments in Fe-Based Metal−Organic Networks. *J. Phys. Chem. C* **2017**, *121*, 4253−4260.

(47) Ma, Y.; Dai, Y.; Wei, W.; Yu, L.; Huang, B. Novel Two- Dimensional Tetragonal Monolayer: Metal−TCNQ Networks. *J. Phys. Chem. A* **2013**, *117*, 5171−5177.

(48) Denawi, H.; Abel, M.; Hayn, R. Magnetic Polymer Chains of Transition Metal Atoms and Zwitterionic Quinone. *J. Phys. Chem. C* **2019**, *123*, 4582−4589.

(49) Denawi, H.; Abel, M.; Siri, O.; Hayn, R. Electronic and magnetic properties of metal-organic polymers with 4d and 5d- transition metal ions. *J. Magn. Magn. Mater.* **2021**, *537*, 168183.

(50) Rochefort, A.; Wuest, J. D. Interaction of Substituted Aromatic Compounds with Graphene. *Langmuir* **2009**, *25*, 210−215.

(51) Shayeganfar, F.; Rochefort, A. Electronic Properties of Self- Assembled Trimesic Acid Monolayer on Graphene. *Langmuir* **2014**, *30*, 9707−9716.

(52) Tada, K.; Tanaka, S.; Kawakami, T.; Kitagawa, Y.; Okumura, M.; Yamaguchi, K. Spin contamination errors on spin-polarized density functional theory/plane-wave calculations for crystals of one- dimensional materials. *Appl. Phys. Express* **2019**, *12*, 115506.

Supplementary Information: Magnetic Signature in Graphene Using Adsorbed Metal-Organic Networks

Alain Rochefort,*,† Khalid N. Anindya,† Xavier Bouju,‡ and Adam H. Denawi¶

†*Département de génie physique, Polytechnique Montréal, Québec, H3C 3A7, Canada*

‡*Centre d'élaboration de matériaux et d'études structurales, CEMES-CNRS, UPR 8011, Université de Toulouse 3 - Paul Sabatier, 29 rue Jeanne Marvig, F-31055 Toulouse, France.*

¶*LPICM, CNRS, École Polytechnique, IP Paris, 91128 Palaiseau, France*

E-mail: alain.rochefort@polymtl.ca

Table S1 contains the results of the different approaches used to determine the magnetic ground state of the C1/G system. First, we noticed that the energy difference between AFM and FM is relatively small, even at PBE+D2 level. As given the size of this model, a total of 172 atoms, the use of PBE0 hybrid-functional with a 25% Hartree–Fock exchange parameter ($\alpha = 0.25$) that is considered the most accurate approach to determine the magnetic ground state of a system remains computationally realistic. The energy difference between AFM and FM found with PBE0 (+4 meV) gives a slightly FM ground states. This constitutes our reference to validate the following DFT+U approach. Then, we compare the results obtained with standard DFT+U technique (non-orthogonalized U projection[1]) from Siesta and QE packages. Both cases give an AFM phase as the ground state, and the energy difference found with Siesta is nearly twice the value obtained with QE. This small discrepancy (22 meV) between Siesta and QE is more probably related to the difference in the methodology used in Siesta (localized orbitals) and QE (plane waves). More importantly, those DFT+U values are not in agreement with the PBE0 reference value. Finally, we used the more recent formulation of Himmetoglu *et al.*[2] for building Hubbard (U) projectors using Lowdin orthogonalized atomic orbitals implemented in QE. For this case, the calculated ground state of C1/G is FM, and the difference from the PBE0 reference is about 1 meV. Consequently, we have adopted this DFT+U approach to evaluate the energy of larger systems, such as C2/G and C3/G.

Table S1: Determination of ground state for the C1/G system. U* means that orthogonalized U projection was used in contrast to non-orthogonalized U projection in DFT+U. All calculations included D2 corrections to account for vdW interactions.

method	E(AFM-FM) (meV)	package
PBE	−1	Siesta
DFT+U	−21	QE
DFT+U	−43	Siesta
DFT+U*	+5	QE
PBE0	+4	QE

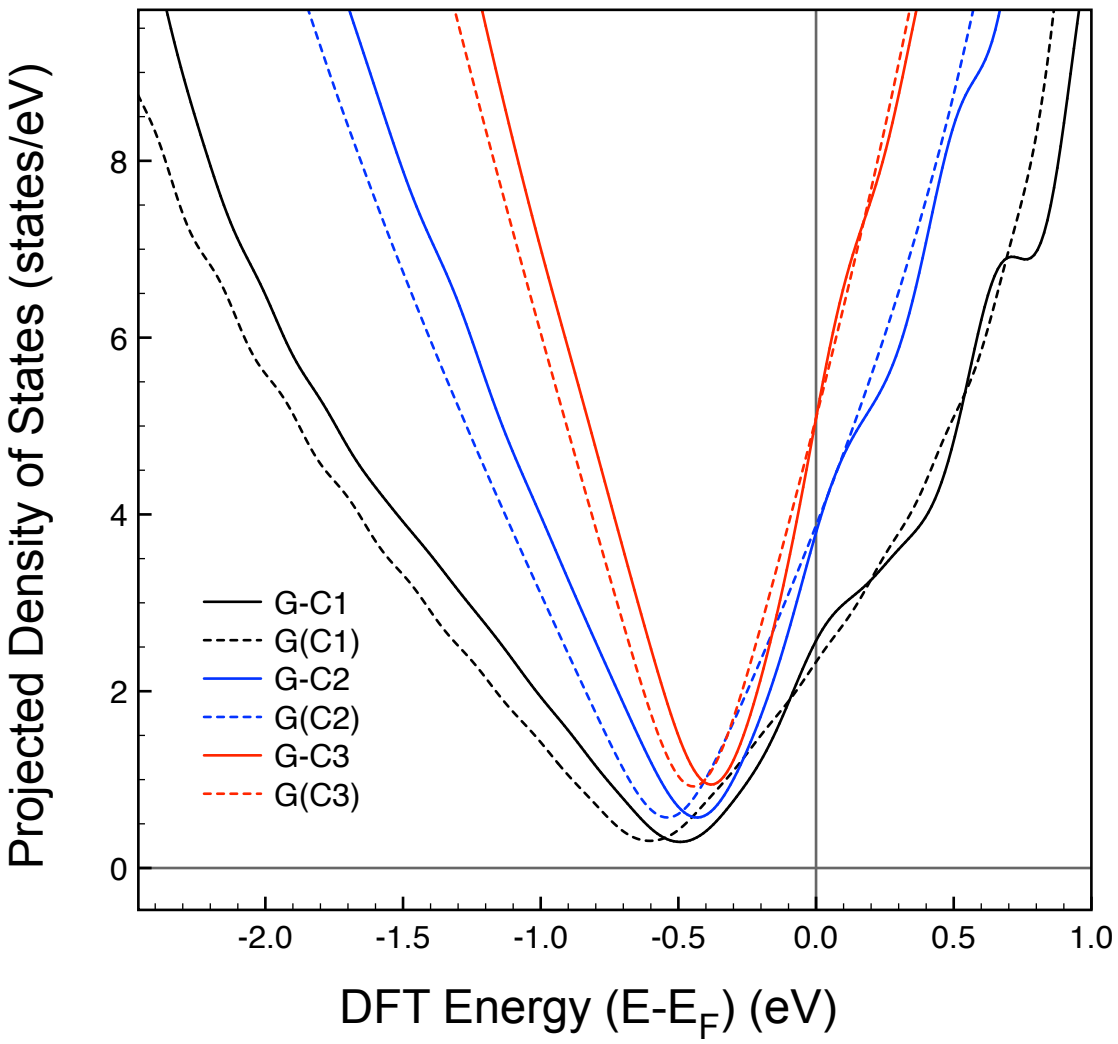

Figure S1: Variation of density of states of free-standing (dashed lines) and stacked graphene (full lines) with the size of the unit cell model. The unit cell of graphene increases as C1 (128 C) < C2 (242 C) < C3 (392 C).

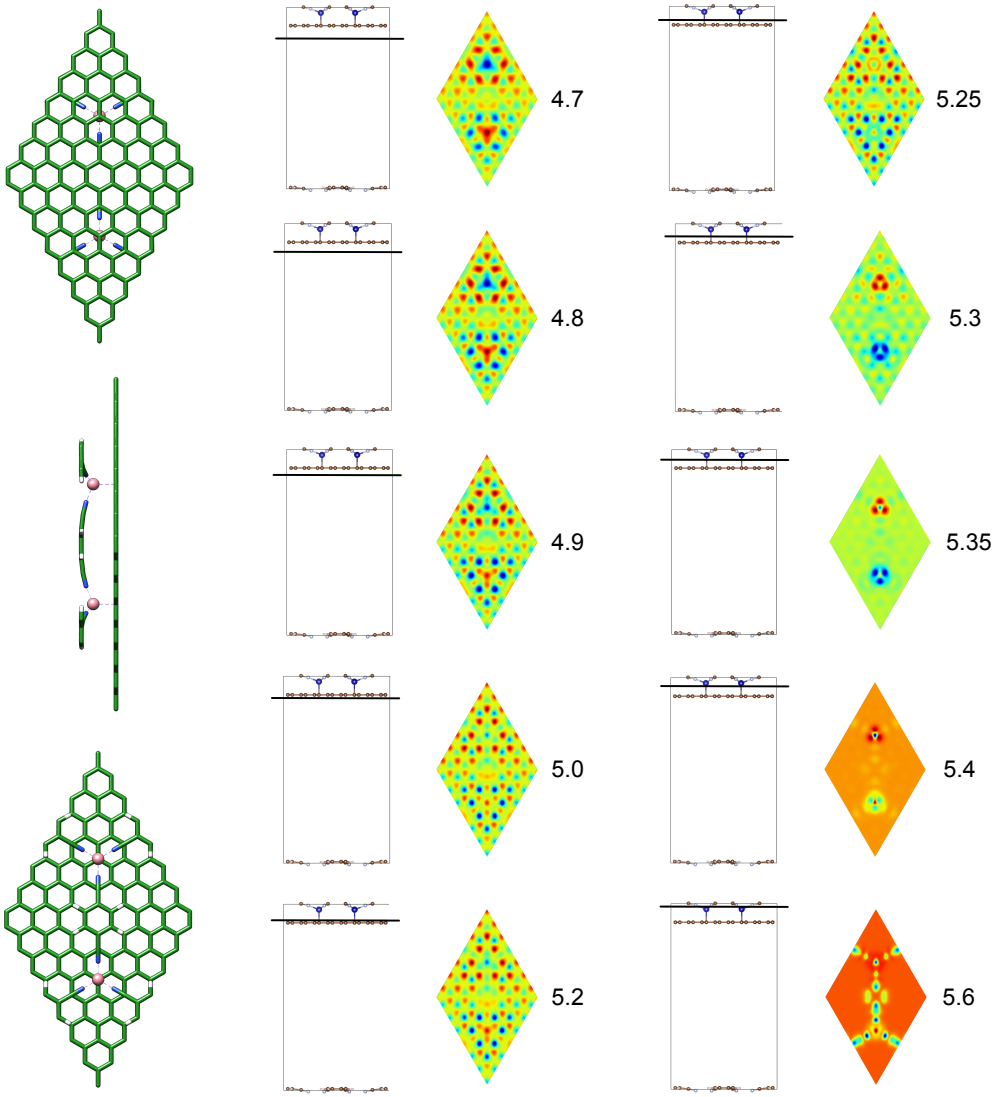

Figure S2: Calculated STM images for various positions (indicated by the black line) in the molecular stack for the AFM phase of the C1/G complex. The color legend is not scaled and is limited by lowest and highest value.

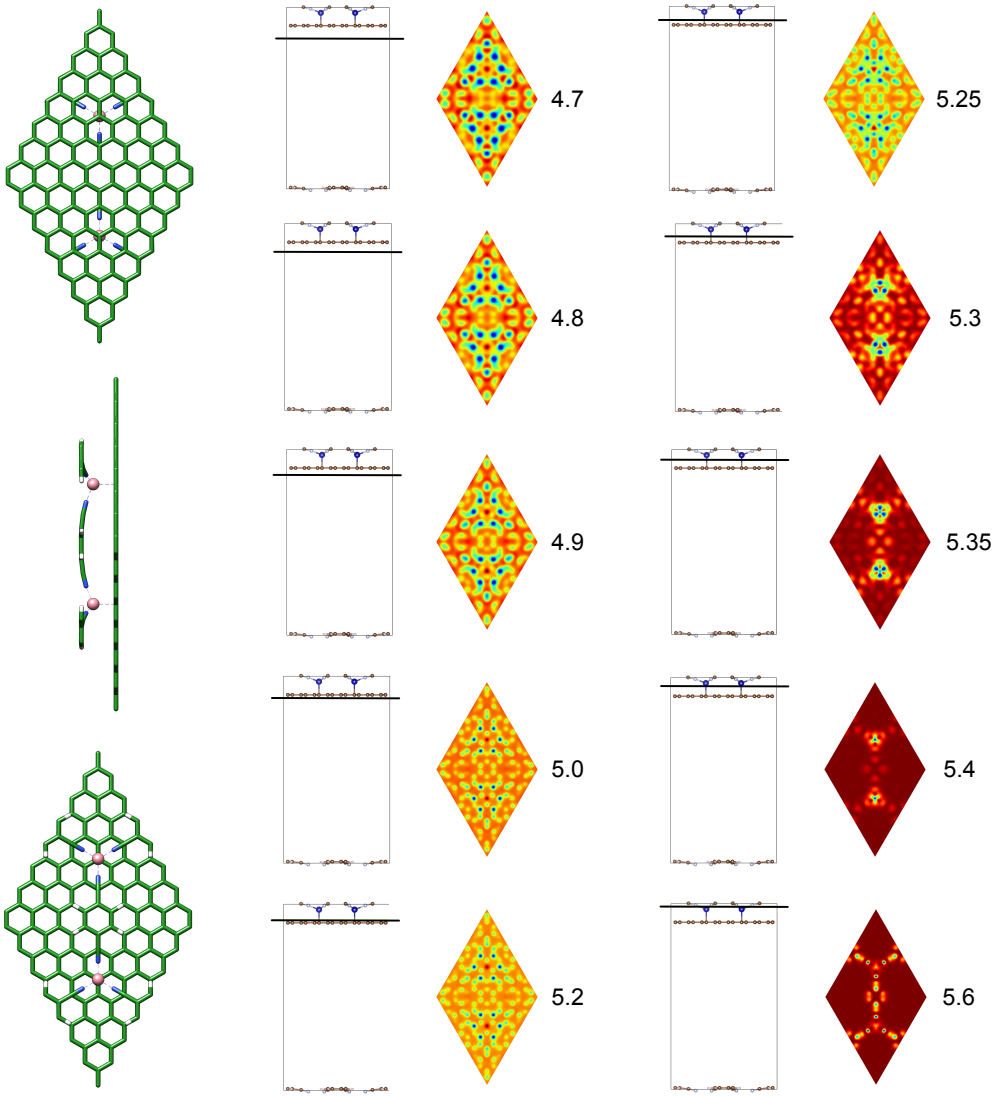

Figure S3: Calculated STM images for various positions (indicated by the black line) in the molecular stack for the FM phase of the C1/G complex. The color legend is not scaled and is limited by lowest and highest value.

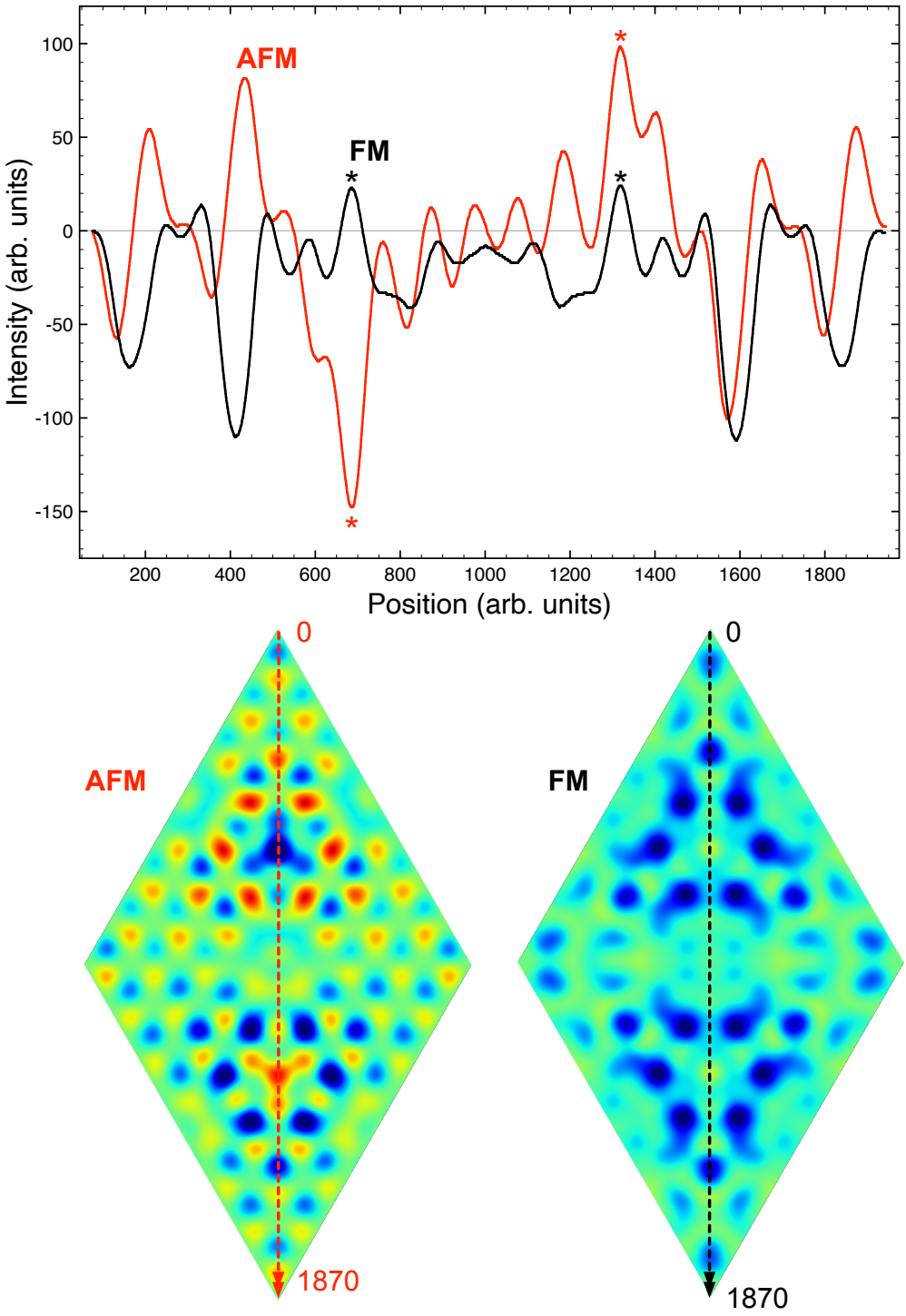

Figure S4: Amplitude profile of STM images for the AFM (red) and FM (black) phases of the C1/G complex according to the path shown in lower panels. The spatial positions of Co atoms are indicated by the stars. A similar arbitrary scale was used for both STM images.

References

(1) Liechtenstein, A. I.; Anisimov, V. I.; Zaanen, J. Density-functional theory and strong interactions: Orbital ordering in Mott-Hubbard insulators. *Phys. Rev. B* **1995**, *52*, R5467–R5470.

(2) Himmetoglu, B.; Wentzcovitch, R. M.; Cococcioni, M. First-principles study of electronic and structural properties of CuO. *Physical Review B* **2011**, *84*, 115108.